Chlorine isotopic compositions of apatite in Apollo 14 rocks: Evidence for widespread vapor-phase metasomatism on the lunar nearside 4 billion years ago

Journal Item

Chlorine isotopic compositions of apatite in Apollo 14 rocks: Evidence for widespread vapor-phase metasomatism on the lunar nearside ~4 billion years ago

Nicola J. Potts[1,2,3*], Jessica J. Barnes[1,4], Romain Tartèse[1,5], Ian A. Franchi[1], Mahesh Anand[1,6]

[1]Planetary & Space Science, The Open University, Walton Hall, Milton Keynes, MK7 6AA, UK

[2]Faculty of Earth & Life Sciences, Vrije Universiteit Amsterdam, De Boelelaan 1085, 1081 HV Amsterdam, NL

[3]School of GeoSciences, King's Buildings, University of Edinburgh, Edinburgh, EH9 3JW, UK

[4] ARES NASA Johnson Space Center, Houston, TX 77058, USA

[5]School of Earth and Environmental Sciences, University of Manchester, Manchester M13 9PL, UK

[6]Department of Earth Sciences, The Natural History Museum, Cromwell Road, London, SW7 5BD UK

*Corresponding author: nicola.potts@ed.ac.uk

ABSTRACT

Compared to most other planetary materials in the Solar System, some lunar rocks display high δ^{37}Cl signatures. Loss of Cl in a H<<Cl environment has been invoked to explain the heavy signatures observed in lunar samples, either during volcanic eruptions onto the lunar surface or during large scale degassing of the lunar magma ocean. To explore the conditions under which Cl isotope fractionation occurred in lunar basaltic melts, five Apollo 14 crystalline samples were selected (14053,19, 14072,13, 14073,9, 14310,171 along with basaltic clast 14321,1482) for *in situ* analysis of Cl isotopes using secondary ion mass spectrometry. Cl isotopes were measured within the mineral apatite, with δ^{37}Cl values ranging from +14.6 ± 1.6 ‰ to +40.0 ± 2.9 ‰. These values expand the range previously reported for apatite in lunar rocks, and include some of the heaviest Cl isotope compositions measured in lunar samples to date. The data here do not display a trend between increasing rare earth elements contents and δ^{37}Cl values, reported in previous studies. Other processes that can explain the wide inter- and intra-sample variability of δ^{37}Cl values are explored. Magmatic degassing is suggested to have potentially played a role in fractionating Cl isotope in these samples. Degassing alone, however, could not create the wide variability in isotopic signatures. Our favored hypothesis, to explain small scale heterogeneity, is late-stage interaction with a volatile-rich gas phase, originating from devolatilization of lunar surface regolith rocks ~4 billion years ago. This period coincides with vapor-induced metasomastism recorded in other lunar samples collected at the Apollo 16 and 17 landing sites, pointing to the possibility of widespread volatile-induced metasomatism on the lunar nearside at that time, potentially attributed to the Imbrium formation event.

1. Introduction

Compared to most other planetary materials in the Solar System, lunar rocks are unique in their wide-ranging chlorine isotopic signatures (Barnes et al., 2016; Boyce et al., 2015; Sharp et al., 2010a; Tartèse et al., 2014a; Treiman et al., 2014). Lunar rocks display $\delta^{37}Cl$ signatures [$^{37}Cl/^{35}Cl$ relative to standard mean ocean chloride (SMOC; 0.31977); Kaufmann et al., (1984)] that range from ~-4 ‰ up to ~+40 ‰, which is in stark contrast to the Earth, where the reported values cluster around 0 ‰ ± 1 ‰ (Barnes et al., 2008; Sharp et al., 2007; Sharp et al., 2013). This deviation in Cl isotope signatures, between the Earth and Moon, is contrary to the isotopic similarity observed for most other elements, including oxygen (Herwartz et al., 2014; Wiechert et al., 2001; Young et al., 2016), calcium (Dauphas et al., 2015; Valdes et al., 2014), chromium (Lugmair and Shukolyukov, 1998), stable chromium (Bonnand et al., 2016), stable strontium (Charlier et al., 2012), silicon (Armytage et al., 2011; Armytage et al., 2012; Zambardi et al., 2013), titanium (Zhang et al., 2012), and zirconium (Schönbächler et al., 2003). Isotopic similarities between the Earth and the Moon have been interpreted that the Moon, most likely, formed from reconsolidation of proto-Earth material after a Moon forming event (Canup, 2012; Canup et al., 2015; Ćuk and Stewart, 2012; Rubie et al., 2015). Thus, Cl isotope fractionation must have occurred during and/or after Moon formation and, therefore, provides unique insight into volatile processing in/on the Moon.

Two competing mechanisms are believed to fractionate Cl isotopes in terrestrial systems: (i) the lighter isotope ^{35}Cl is preferentially vaporized (Graham's Law), in volcanic gases for example, while (ii) the heavier ^{37}Cl becomes incorporated into HCl(g) as a result of its relatively high bond strength (Schauble et al., 2003) in systems where H>>Cl (Sharp et al., 2010a). Most bulk primitive terrestrial basalts measured to date have $\delta^{37}Cl$ values clustering

around ~0 ± 2 ‰, suggesting that these two fractionation mechanisms cancel each other out in terrestrial systems (Sharp et al., 2013). To explain the elevated $\delta^{37}Cl$ values (i.e. > 0 ‰) of lunar samples, Sharp et al. (2010a) favored the hypothesis in which lunar basaltic melts were characterized by H<<Cl, which promoted the degassing of Cl as metal chlorides (e.g., NaCl, etc.) instead of HCl(g). This process would have preferentially incorporated the lighter isotope ^{35}Cl into the degassed metal chloride phase, resulting in residual melts that were enriched in ^{37}Cl (Sharp et al., 2010a).

Subsequent studies, of chlorine isotopes in lunar apatite, argued that preferential outgassing of ^{35}Cl from erupting lavas was unlikely to be the main driver for the large Cl isotope fractionation in lunar melts, notably because (i) apatite in plutonic samples tend to have higher $\delta^{37}Cl$ values than apatite in erupted volcanic samples, and (ii) there seems to be a broad positive correlations between chlorine isotopes and abundances (Boyce et al., 2015; Barnes et al., 2016). Indicating that whatever mechanism(s) caused the extreme fractionation of chlorine isotopes must have been capable of producing a reservoir that is rich in Cl, and is characterized by an elevated Cl isotopic composition (Boyce et al., 2015). This assumption, and dismissal of degassing as the mechanism for Cl isotope fractionation, is only valid if all samples had the same initial Cl concentration and $\delta^{37}Cl$ value; a highly unlikely scenario.

In addition, positive correlations between apatite $\delta^{37}Cl$ values and some bulk-rock trace element characteristics, such as La/Lu ratios and Th contents (Barnes et al., 2016; Boyce et al., 2015), have been used to suggest heavy $\delta^{37}Cl$ are somehow linked to the involvement of a KREEP (potassium (K), rare earth elements (REE), phosphorous (P); (Warren and Wasson, 1979) component. Boyce et al. (2015) attributed large-scale Cl isotope fractionation to the

degassing of metal chlorides from the molten lunar magma ocean (LMO). In their model, the elevated $\delta^{37}Cl$ values recorded by apatite, within the mare basalts, would have been acquired during assimilation of a KREEP-component either (i) into the mare basalt source regions or (ii) as the basalts ascended towards the lunar surface. While Barnes et al. (2016) suggested that the ~34 to ~43 km of lunar crustal material (Wieczorek et al., 2013) was sufficiently thick to prevent loss of Cl-bearing species from the LMO via continuous degassing, especially given the high solubility of Cl in basaltic melts (Webster et al., 2009). Instead, they proposed that crust-breaching impact events exposed KREEP-rich melt to low pressure environments, promoting degassing of metal chlorides, and subsequent Cl isotope fractionation (Barnes et al., 2016).

One of the heaviest lunar $\delta^{37}Cl$ values measured to-date, ~ +32 ‰, is from the granulite sample 79215, whose signature is not thought to be from any process described above (Treiman et al., 2014). This sample is characterized by an elevated P content (~200 × CI chondrite P contents) but low K or REE contents (~10 × CI; e.g., P/Sm = ~20Treiman et al. (2014) suggested that in 79215, P, and the halogens, were largely added during vapor-phase metasomatism, likely originating from impact-induced devolatilization of a KREEP-rich target. Vapor-phase metasomatism is favored given that lunar conditions are too reduced for abundant H_2O or CO_3^{2-} to be present and the lack of supporting evidence for fluid metasomatism in lunar samples This suggest that surface processes can also be responsible for modifying Cl isotope composition in lunar samples.

Detailed understanding of the individual petrological histories of the rocks investigated in Cl isotope studies is, therefore, critical to deciphering the mechanism(s) by which Cl isotopes may have fractionated in lunar samples. In order to investigate the potential processes that

contributed to the elevated $\delta^{37}Cl$ values observed in lunar apatite, five Apollo 14 samples were studied: high-Al basalts 14053 and 14072, a basaltic clast from breccia 14321,1482 and impact melt rocks 14073 and 14310. These Apollo 14 samples have distinct petrogenetic histories, and all pre-date the main period of mare volcanism, providing unique insight into the timing of, and process(es) responsible for, Cl isotope fractionation in/on the Moon. Furthermore, the high modal abundance and large size (typically > 50 μm in the longest dimension) of apatite grains in these samples permitted a thorough investigation of intra-grain and inter-sample variations in volatile abundances and Cl isotope systematics.

2. Apollo 14 High-Al rocks

The Apollo 14 mission landed on the Fra Mauro Formation, which is part of the ejecta blanket that formed from the excavation of the Imbrium Basin (Nemchin et al., 2009; Snape et al., 2016). Mare Imbrium is the largest basin-affiliated mare deposit on the Moon (assuming that the Procellarum KREEP Terrane is not an impact feature), and is thought to have excavated lower lunar crust material during the basin-forming event (Nemchin et al., 2009). It remains unclear, however, which Apollo 14 samples represent true Imbrium ejecta and which are locally derived (Hiesinger and Head, 2006). The consistent dates obtained by $^{40}Ar/^{39}Ar$ dating on whole rocks and fines (Alexander and Davis, 1974; Turner et al., 1972; Turner et al., 1971) and Rb-Sr dating (Papanastassiou and Wasserburg, 1971; Compston et al., 1972; Compston et al., 1972) of ~3.87 Ga were interpreted as representing the timing of formation of the Imbrium Basin (Stöffler and Ryder, 2001; Wilhelms et al., 1987). Recent high-precision U-Pb dating of phosphates and zircons in Apollo 14 impact melt breccias has provided an improved estimate for the formation of the Imbrium Basin at ~3.93 Ga (Snape et al., 2016, and references therein). Other studies of zircon grains from Apollo 14 lunar breccias have yielded U-Pb dates ranging from ~4.0 to ~4.4 Ga, with distinct date peaks at ~4.35 and ~4.20 Ga (Meyer et al., 1996;

Nemchin et al., 2008), suggesting that a significantly older pre-Imbrium history is recorded by the breccias. The temperature and shock effects associated with the development of the Fra Mauro Formation were, therefore, sufficient to reset $^{40}Ar/^{39}Ar$ and Rb-Sr dates but not to reset the zircon U-Pb systems in all samples (Nemchin et al., 2010).

Some basalts from the Fra Mauro region record volcanism older than 4 billion years on the Moon (Neal and Kramer, 2006). Basaltic clasts from this region indicate a period of ~400 million years of volcanism, from ~4.3 to ~3.9 Ga (Compston et al., 1972; McKay et al., 1979; Papanastassiou and Wasserburg, 1971; Snape et al., 2016), pre-dating the main period of mare volcanism (Snyder et al., 2000). Volcanics from the Fra Mauro region may provide insights into the evolution of the Moon from solidification of the crust, at around ~4.5 Ga to ~4.3 Ga (Elkins-Tanton et al., 2011), to the beginning of the main period of mare volcanism that commenced around ~3.85 Ga (Shearer et al., 2006). Crystallization and/or impact-resetting ages for all the Apollo 14 samples studied here are given in Table 1, and range between ~4.1 Ga and ~3.8 Ga (Compston, et al., 1972; Dasch et al., 1987; Hui et al., 2013; Husain et al., 1971; Mark et al., 1974; Papanastassiou and Wasserburg, 1971; Tatsumoto et al., 1972; Turner et al., 1972; York et al., 1972).

In addition to their old age, the Apollo 14 basalts are also geochemically distinct in that they are relatively enriched in Al_2O_3 (11 – 16 wt.%), leading to their classification as 'high-Al' basalts (Neal and Kramer, 2006; Ridley, 1975). Two petrological models have been proposed for the formation of these high-Al samples: (1) "pristine" volcanic rocks that formed solely through endogenous lunar processes and (2) impact generated melts referred to as "impact melts" (Hui et al., 2011).

Based on incompatible trace element (ITE) abundances and crystallization ages, the Apollo 14 high-Al basalts have been separated into three distinct groups: Group A (~4.3 Ga), Group B (~4.1 Ga), and Group C (~3.9 Ga) (Neal and Kramer, 2006). Samples within these groups are thought to be related via a closed-system crystal fractionation model for Group A, and an open-system evolution model, involving assimilation of a KREEP component and/or granitic melts, for Groups B, and C (Hui et al., 2011; Neal et al., 1988; Neal et al., 1989; Neal and Kramer, 2006; Neal and Taylor, 1989). The main geochemical features of the samples studied here are summarized in Table 1. The impact-melt samples, 14073 and 14310, are crystallization products of impact-melted lunar regolith and/or feldspathic crust (Schonfeld and Meyer, Charles, 1972), and could have inherited their high-Al contents from melting of anorthosite-rich targets (Hui et al., 2011). In contrast, for the endogenous pristine basalts (14053, 14072, and 14321,1482), the high-Al content is not related to any contribution from the melting of anorthosite-rich rocks and it is more likely that elevated Al contents were directly inherited from the mantle source regions of these basalts (Hui et al., 2011; Neal and Kramer, 2006). These different formational mechanisms have been used to explain the compositional differences between the Apollo 14 pristine basalts and impact melt samples. Detailed descriptions of all the samples studied here is given in the Supplementary Material.

3. Analytical techniques

Before secondary ion mass spectrometry (SIMS) measurements, each polished thin-section was carbon-coated and studied using a dual beam FEI Quanta 3D Scanning Electron Microscope (SEM) at The Open University, following the protocol described in Tartèse et al. (2013). The SEM was used to locate apatite crystals suitable for SIMS analyses, and to characterize the petrographic context of each grain. The carbon coat was removed after SEM work and the samples were cleaned with isopropanol and stored in a vacuum oven at ~55 °C

for a minimum of 48 hours. Subsequently, samples were coated with ~30 nm of gold using an EMITECH K575X peltier cooled gold sputter coater. After coating, the samples were immediately loaded into the Cameca NanoSIMS 50L at The Open University. Apatite was located following initial pre-sputtering for several minutes of large (>10 × 10 μm) areas. Smaller ~8 × 8 μm areas, containing the target apatite grains, were then pre-sputtered by rastering a Cs^+ beam of ~40 pA with an accelerating voltage of 16 kV for ~2 minutes, in order to clean the target surface. For analysis, the 40 pA probe was then rastered over ~4 × 4 μm areas in the apatite grains for ~4 minutes. An electron flood gun was used for charge compensation. During analysis the vacuum in the analysis chamber remained around ~5×10^{-9} Torr. The NanoSIMS was tuned to achieve a mass resolving power of ~8000 and the negative secondary ions of $^{16}O^1H$, ^{18}O, ^{19}F, ^{35}Cl, ^{37}Cl, and $^{40}Ca^{19}F$ were collected simultaneously on electron multipliers. ^{19}F ions were monitored, but only for ~66s per analysis to avoid saturating the detectors.

The abundances of Cl, F, and H_2O were calibrated using the published Cl, F, and H_2O contents and the measured $^{35}Cl/^{18}O$, $^{19}F/^{18}O$, and $^{16}OH/^{18}O$ ratios of Ap004 and Ap018 reference apatite crystals mounted in epoxy resin (McCubbin et al., 2012). Background measurements of Cl and OH were collected on San Carlos olivine and nominally anhydrous minerals within sample sections (~100 ppm H_2O and ~4 ppm Cl) and were subtracted from the measured values. Reported uncertainties for abundances incorporate the 2σ uncertainty of the calibration slopes and analytical uncertainties associated with individual measurements. Ap004 was used to correct the measured $^{37}Cl/^{35}Cl$ ratios of unknown samples for instrumental mass fractionation (IMF; $(^{37}Cl/^{35}Cl_{unknown}/^{37}Cl/^{35}Cl_{standard})-1)*1000$). The Cl isotope composition is reported using standard delta notation with respect to $^{37}Cl/^{35}Cl$ of standard mean ocean chloride. Isotope measurements are reported with their associated 2σ uncertainties, which

combine the reproducibility of the $^{37}Cl/^{35}Cl$ measurements on an appropriate standard and the internal uncertainty of each analysis.

4. Results

In the following section, textural descriptions and $\delta^{37}Cl$ values of apatite, with corresponding Cl and H_2O abundances, are given for each sample. High-resolution back-scattered electron (BSE) images including the petrographic setting of individual apatite grains analyzed in this study are shown in Supplementary Figures SM2 to 6. The results of NanoSIMS analyses of apatite for Cl isotopic compositions and H_2O and Cl abundances are listed in Table 2. In addition F abundances for apatite in some samples are listed in Table 2.

4.1. 14053,19

In sample 14053,19 eight analyses were carried out in seven apatite crystals occurring in four separate areas (Fig. SM2A-D). Apatite crystals in this sample are all associated with mesostasis. Here, mesostasis regions were identified by the breakdown of fayalite into Fe metal (often described as 'spongy' Fe in the literature (Taylor et al., 2004)) and silica-rich glass, as well as the presence of a diverse range of phases with relatively small grain sizes (<20 μm in the longest dimension; Potts et al., 2016). All of the apatite grains measured here were subhedral to anhedral, >10 μm in the longest dimension, and were found associated with quenched K-rich glass. The majority of apatite grains in this section were also found in contact with plagioclase, except Ap#4a and Ap#4b.

The volatile abundances of apatite in 14053 overlap with those of Mg- and alkali- suite rocks (Fig. 1), which are fluorapatite with greater amounts of Cl than H_2O. The $\delta^{37}Cl$ values of apatite in 14053,19 range from +15.6 ± 2.2 ‰ to +34.3 ± 2.9 ‰. H_2O abundances of apatite in this sample range from 89 ± 4 ppm to 1662 ± 80 ppm (Fig. 2A; Table 2). The Cl concentrations of apatite in this sample range from 1569 ± 2 ppm to 16054 ± 17 ppm (Fig. 2B; Table 2). Apatite 4a shows the highest $\delta^{37}Cl$ value (+34.3 ± 2.9 ‰) whilst having the lowest H_2O content (89 ± 4 ppm) and highest Cl content (16054 ± 17 ppm) of any apatite measured from this sample. In contrast, Ap#1 has the lowest $\delta^{37}Cl$ value (+15.6 ± 2.2 ‰) measured from this sample and the highest H_2O content (1662 ± 80 ppm) and lowest Cl content (1569 ± 2 ppm). Both apatite crystals Ap#4a and Ap#1 are found within mesostasis regions although there appears to be significantly more fayalite reduction surrounding Ap#4a than Ap#1. Overall, there are strong correlations between increasing $\delta^{37}Cl$ values and (a) decreasing H_2O abundances and (b) increasing Cl abundances for apatite in 14053,19 (Fig. 2A-B). There is little intra-region variation, in terms of $\delta^{37}Cl$, in this section except for Area #1 in which the two analyses yielded a difference of ~12 ‰. The two heaviest values (> +32 ‰) in this section are from two apatite grains within the same region (area 4), which displays the highest proportion of reduction-related texture. Apatite grains in this region also display resorbed edges compared to apatite within areas 1 and 5 that are characterized by $\delta^{37}Cl$ values around +23 to +28 ‰ (except Ap#1). Apatite grains within area 8 also appear to have resorbed edges, and have $\delta^{37}Cl$ values of between +21 and +24 ‰. The subhedral apatite grains within areas 1 and 5 have higher H_2O contents (>500 ppm) compared to the andehral apatite grains within area 4 (<200 ppm). The highest Cl contents have been measured in the subhedral grains found in area 4.

4.2. 14072,13

In sample 14072,13 five analyses were carried out in five distinct apatite crystals occurring in four different areas (Fig. SM3A-E where B and C are both part of one larger area). All apatite crystals were found within mesostasis regions that were texturally similar to those in 14053,19, although mesostasis regions in 14072,13 generally contained a larger fraction (>30 modal %) of spongy Fe. Large (> 20 μm) euhedral to sub-euhedral apatite yielded $\delta^{37}Cl$ values ranging from +16.3 ± 2.9 ‰ to +40.0 ± 2.9 ‰, with Cl and H_2O abundances ranging from 4167 ± 5 to 14759 ± 15 ppm and 117 ± 6 to 189 ± 9 ppm, respectively (Figs. 2A-B; Table 2).

The volatile abundances of apatite in this thin-section overlap with those of Mg- and alkali-suite rocks (Fig. 1). Unlike sample 14053,19, there is no clear correlation between apatite Cl or H_2O abundance and the associated $\delta^{37}Cl$ values in 14072,13 (Fig. 2). All of the apatite grains, except in area 7, are in contact with spongy Fe- and K-rich glass, while the mesostasis pockets are surrounded by plagioclase. The lower $\delta^{37}Cl$ values of around +16 to +20 ‰ have been measured in euhedral apatite grains, while the heaviest $\delta^{37}Cl$ values (+28.8 ± 2.9 ‰ and +40.0 ± 2.9 ‰) are associated with anhedral crystals. This relationship is broadly consistent with what we observed in sample 14053,19.

4.3. 14321,1482

In sample 14321,1482 four analyses were carried out in three apatite crystals occurring in three different areas (Fig. SM4A-C). Apatite crystals in 14321,1482 are euhedral to subhedral, > ~10 μm in the longest dimension, and were located in mesostasis regions, which contain spongy Fe in areas 3 and 5, fayalite, silica, and K-rich glass.

The apatite $\delta^{37}Cl$ values range from +20.1 ± 0.9 ‰ to +28.6 ± 1.1 ‰ and are associated with Cl abundances of ~5000-8000 ppm and very low H_2O contents < 150 ppm (Figs. 2A-B; Table 2). Although limited in number, the analyses of 14321,1482 are consistent with the ranges of Cl abundances and $\delta^{37}Cl$ values measured in most of the apatite grains from samples 14053 and 14072. The lowest $\delta^{37}Cl$ value in this sample has been measured in area 5 on an anhedral apatite grain in this section, opposite to observations for 14053 and 14072. This grain also is in direct contact with spongy Fe. The other apatite grains within this sample have $\delta^{37}Cl$ values between ~ +24 and +29 ‰ and are all euhedral to subhedral.

4.4. 14073,9

In sample 14073,9 fifteen analyses were carried out on nine apatite crystals occurring in five different areas (Fig. SM5A-E). All apatite grains in this sample were located in mesostasis regions, identified by the presence of K-rich glass. The mesostasis regions in 14073, however, are texturally and compositionally different from those in 14053 and 14072, as they do not contain spongy Fe, but interstitial K-rich glass associated with K-feldspar. The apatite grains analyzed here are subhedral, up to 50 μm in the longest dimension, and are all in contact with K-rich glass, with some containing melt inclusions.

The analyzed apatite grains are H_2O-poor and Cl-rich compared to typical mare basalts (Fig. 1). The $\delta^{37}Cl$ values of apatite from sample 14073,9 display a large range from +16.5 ± 2.2 ‰ to +36.9 ± 2.1 ‰, most of the them clustering between ~ +21 and +28 ‰ (Fig. 2A-B). The Cl and H_2O abundances of these apatite range from 580 ± 1 ppm to 16149 ± 18 ppm and

291 ± 14 ppm to 1081 ± 52 ppm, respectively. Generally, the higher $\delta^{37}Cl$ values correspond to low to moderate H_2O contents, while there is no strong correlation between $\delta^{37}Cl$ values and Cl abundances (Fig. 2). In some mesostasis areas, such as area 11 (a cluster of apatite crystals) in which 5 analyses were carried out, apatite crystals are fairly homogeneous in terms of abundances of H_2O (317 ± 15 ppm to 419 ± 20 ppm) and Cl (1241 ± 2 ppm to 1648 ± 2 ppm) and Cl isotopic composition (+21.0 ± 2.2 ‰ to 27.5 ± 2.6 ‰). In other areas, the intra-region variations of $\delta^{37}Cl$ are large, ranging from +16.5 ± 2.2 ‰ to +27.7 ± 2.0 ‰ within a single apatite grain (Ap#12), and between +25.7 ± 1.9 ‰ and +36.9 ± 2.1 ‰ in a single grain analyzed in area 19.

4.5. 14310,171

Seven analyses were made across four apatite crystals in three areas (Figs. SM6A-C) in thin section 14310,171. Generally apatite was found in mesostasis regions in this sample, although these areas noticeably lack the large amount of K-rich glass observed in other Apollo 14 mesostasis regions, particularly 14073,9. The apatite grains in 14310,171 are euhedral to subhedral, with the size varying from > ~30 μm to ~10 μm in the longest dimension. Apatite is associated with pyroxene, plagioclase, K-feldspar, merrillite, and ilmenite. The $\delta^{37}Cl$ values for apatite in this sample range from +14.6 ± 1.6 ‰ to +25.3 ± 2.0 ‰, and apatite Cl and H_2O abundances range from 4597 ± 8 ppm to 11256 ± 19 ppm and 95 ± 3 to 354 ± 11 ppm, respectively (Table 2). Similarly to apatite in sample 14073,9, elevated $\delta^{37}Cl$ values tend to be associated with lower H_2O abundances (Fig. 2A). In this sample, the higher $\delta^{37}Cl$ values also tend to be associated with higher Cl abundances (Fig. 2B). As in sample 14073,9, the degree of intra-region heterogeneity in $\delta^{37}Cl$ values varies across the sample, particularly in area 4. The euhedral apatite grains in this section have the lower $\delta^{37}Cl$ values (< +18 ‰), while the

heavier Cl isotope values are associated with a smaller (<10 μm) subhedral apatite grain, apart from those in area 1.

5. Discussion

This study provides a comprehensive dataset on the chlorine isotopic compositions of apatite from Apollo 14 samples, including both igneous high-Al basalts and impact melt rocks. As shown in Figure 3, the δ^{37}Cl values measured here mostly cluster within a range of between +15 and +35 ‰, which is consistent with the upper end of the range of δ^{37}Cl values measured in high- and low-Ti mare basalts and with those obtained on KREEP-rich samples (Barnes et al., 2016; Boyce et al., 2015; Sharp et al., 2010a; Tartèse et al., 2014a; Treiman et al., 2014). The heaviest δ^{37}Cl values, of around +35 to +40 ‰, were measured in apatite from samples 14053, 14072, and 14073 and are comparable to the heaviest δ^{37}Cl values reported for KREEP-rich basalts (Sharp et al., 2010a; Barnes et al., 2016) and KREEP-rich instrusive rocks of the Mg-suite (Treiman et al., 2015; Barnes et al., 2016). The unique petrogeneses of the Apollo 14 samples studied here provide an opportunity to evaluate the potential mechanisms for Cl isotope fractionation under lunar magmatic conditions.

5.1. Linking assimilation of KREEP to the Cl isotope composition of magmatic apatite

Magmatic degassing of chlorine from the LMO, in the form of metal chlorides, has been invoked to explain the elevated chlorine isotopic compositions of lunar samples (Boyce et al., 2015; Barnes et al., 2016). This hypotheses results in an enrichment of ^{37}Cl in the KREEP-rich residual melts of the LMO, and is supported by the positive correlations observed between bulk-rock incompatible trace element contents (REE, Th) and apatite δ^{37}Cl values (Fig. 4). Our analyses of apatite in five Apollo 14 samples, however, do not show any correlation between

KREEP component (e.g. elevated La/Lu ratios in bulk samples) and elevated $\delta^{37}Cl$ values (Fig. 4). Petrologically, the high-Al pristine basalts 14053, 14072, and 14321,1482 are all believed to have assimilated an evolved KREEP-rich component even though they are not *sensu stricto* KREEP-basalts (Hui et al., 2011; Neal et al., 1988; Neal and Kramer, 2006). The impact melt samples 14073 and 14310 also contain a significant KREEP component (El Goresy et al., 1971; McKay et al., 1979) but are thought to have formed via the melting of feldspathic regolith or anorthosite material (Hui et al., 2011; Schonfeld et al., 1972). The Apollo 14 samples studied here thus suggest that additional magmatic and/or post-crystallization processes can modify apatite $\delta^{37}Cl$ values.

5.2. Volatile abundances in Apollo 14 apatite

All of the apatite analyzed here are F-rich, with compositions clustering around the F apex of the apatite volatile ternary (Fig. 1). Volatile compositions of apatite in samples 14072, 14310, and 14321,1482 plot almost exclusively along the F-Cl binary, in the field typically occupied by apatite from lunar highland samples. Apatite compositions for 14053 and 14073 have a greater H_2O component, consistent with the apatite compositions of KREEP-rich basalts and relatively H_2O-poor mare basalts (Barnes et al., 2014, 2013; Boyce et al., 2010; Greenwood et al., 2011; McCubbin et al., 2015b, 2011, 2010a, 2010b; Tartèse et al., 2014; Tartèse et al., 2013; Tartèse et al., 2014b).

The range of measured water contents within apatite in high-Al basalt 14053 (~90 - 1660 ppm H_2O) is similar to the range obtained in previous studies of this sample, from around 200 ppm up to ~2400 ppm H_2O (Greenwood et al., 2011; Boyce et al., 2010; McCubbin et al., 2010; Pernet-Fisher et al., 2014). Similarly, previously measured apatite Cl contents of ~0.17 to 0.47

wt.% in 14053 (Boyce et al., 2010; McCubbin et al., 2010) are within the range of apatite Cl abundances measured here (~0.16 to 1.6 wt.%).

Determining the volatile content of the melt from which apatite crystallized, based on the measured volatile contents of apatite, is not trivial given that F, Cl, and OH (reported here as H_2O) share the crystallographic *X*-site within the apatite crystal lattice. As such, volatiles are essential structural components, meaning that simple Nernst partitioning behavior cannot be applied (Boyce et al., 2014; McCubbin et al., 2015). Apatite, however, is generally considered a major sink for F in crystallizing melts (McCubbin, et al, 2015) as crystal chemistry favors preferential incorporation of F, over OH and Cl, into apatite (Boyce et al., 2014; Kusebauch et al., 2015). As F is incorporated into apatite and/or lost via degassing (Ustunisik et al., 2015; Ustunisik et al., 2011), total F in the melt would decrease with crystallization, meaning primary apatite would have higher F contents than later grown apatite. If all the samples began with similar F melt content and Cl isotope ratios, this could suggest that apatite with greater F abundances record the initial $\delta^{37}Cl$ values of their respective melts. Apatite grains with lower F abundance would, therefore, have grown later and record the $\delta^{37}Cl$ isotopic compositions of the melt at the more advanced stages of crystallization. There is a vague correlation between increasing $\delta^{37}Cl$ values and decreasing F abundance of apatite (Fig. 5). In sample 14321,1482 there are very few F measurements, so we cannot ascertain whether we have analyzed early growing apatite, there is only one stage of apatite growth, or there is no change in apatite F contents (and Cl isotope signatures) with melt evolution. For 14310, there is some correlation between F abundances and $\delta^{37}Cl$ values (Fig. 5). Overall, the rough trend displayed by most apatite analysis in samples 14053, 14072, and 14073 could suggest that the initial $\delta^{37}Cl$ values of the Apollo 14 melts were around ~20 ± 5 ‰ and that subsequent melt evolution has imparted heavier $\delta^{37}Cl$ signatures. It is important to stress that this interpretation is only valid if F

contents and Cl isotope ratios were similar throughout different melts. The different petrogeneses of these samples also suggests it is unlikely they began with the same volatile abundance and isotope signatures. Importantly, however, if crystal chemistry controls dominate apatite compositions, then the chlorine isotopic compositions of apatite can only be explained by increasing the $^{37}Cl/^{35}Cl$ of the melt, or apatite after crystallization.

5.3. Solar-wind implantation

Apollo 14 sample 14053 is thought to have crystallized as a typical high-Al basalt, but the outer sections were later affected by solar-wind H implantation during its residence in the lunar regolith (Taylor et al., 2004). Subsequently, subsolidus thermal metamorphism (likely induced from ejecta blanket heat) facilitated the permeation of solar-wind H into the rock and led to reduction of localized areas, characterized by reduction-breakdown textures of fayalite to Fe-metal and silica, identified by the below reaction (Taylor et al., 2004).

$$Fe_2SiO_4 + 2H_2 = 2Fe^o + SiO_2 + 2H_2O\uparrow$$

These reduction-breakdown textures, identified by the presence of Fe-metal and silica, are shown in Figures SM2A, 2B, and 2D. Reduction-breakdown textures are also seen in 14072, and to a smaller extent in 14321,1482. It has also been suggested that La_2O_3 and Ce_2O_3 contents in apatite from 14053, in contact with reduced areas, may have undergone secondary alteration as a consequence of H-reduction (Taylor et al., 2004). If such metamorphism occurred then it is conceivable that the volatile abundances and isotopic composition of apatite in these samples may have been modified (Boyce et al., 2010; Greenwood et al., 2011).

The lack of reduction textures in 14310 and 14073 is important given that these rocks formed from impact melt processing of the lunar regolith, indicating that either (i) such a signature was erased during impact melting or (ii) that these samples did not undergo the surface reduction process, unlike the other samples studied. The second scenario would support late alteration of 14053 (and potentially 14072, as well as 14321,1482) and negligible solar-wind alteration of 14310 and 14073.

5.4. The role of volatile degassing from lunar magmas

Chlorine is incompatible in the major silicate minerals that crystallize from basaltic melts (e.g. Webster et al., 2009). When Cl reaches saturation it will partition into the vapor phase, and degas from basaltic melts (Boyce and Hervig, 2008; Patiño Douce and Roden, 2006; Shinohara, 2009; Ustunisik et al., 2011; Ustunisik et al., 2015; Webster et al., 1999). Sharp et al. (2010b) suggested that under anhydrous lunar magmatic conditions the bonding potentials of both isotopes (^{35}Cl and ^{37}Cl) are similar. The kinetic loss of ^{35}Cl is not cancelled out by the loss of ^{37}Cl via bond incorporation (e.g. $HCl_{(g)}$). The melt is then enriched in ^{37}Cl explaining the heavy $\delta^{37}Cl$ values acquired by late-crystallizing apatite. Theoretical modeling of Cl isotope fractionation during degassing of metal chloride species indicates that a $\delta^{37}Cl$ increase of up to 20 ‰ is expected for 95% Cl loss as $FeCl_2$ (Sharp et al., 2010a; Ustunisik et al., 2015), which could explain the range in $\delta^{37}Cl$ values exhibited by apatite from most mare basalt samples (Barnes et al., 2016; Boyce et al., 2015; Sharp et al., 2010a; Tartèse et al., 2014a). It is important to note that the H << Cl conditions required in the Sharp et al. (2010a) model does not necessarily imply that lunar melts were dry, but it does require melt H << Cl at the time of Cl degassing. It should also be noted that other lines of evidence for magmatic degassing from lunar melts is recorded in the literature, through coatings on glass beads (McKay et al., 1972),

fractionations of H (Hauri et al., 2015 and references therein), and C (Wetzel et al., 2015) isotope systems. The large inter- and intra-sample $\delta^{37}Cl$ variations measured in apatite across Apollo samples, with vastly different petrogenesis seem difficult.

5.5. Vapor-phase interactions

Near-surface fractionation of Cl isotopes via Cl evaporation (as HCl, as well as organic and metal compounds) has been suggested as a potential mechanism to induce fractionation in terrestrial systems (Gola et al., 2005), which is supported by modelling (Richet et al., 1977), as well as experimental work (Huang et al., 1999; Liebscher et al., 2006), and thought to be responsible for elevated signatures (~32 ‰) in lunar granulite 79215 (Treiman et al., 2014). It is, therefore, conceivable that a volatile-rich vapor, enriched in ^{37}Cl, interacted with the late-stage Apollo 14 basaltic and impact melts, similar to what has been proposed by Treiman et al. (2014) to account for elevated apatite $\delta^{37}Cl$ values in granulite 79215. Vapor phase crystallization of a variety of minerals, including oxides, halides, iron, and alkali, has been reported in vugs within Apollo 14 breccias (McKay et al., 1972). This vapor phase, noted to have contained chlorides, has been attributed to thermal metamorphism immediately following the deposition of the Fra Mauro ejecta blanket from the Imbrium Basin (McKay et al., 1972), the source of which would be a volatile-rich rock in the shallow crust. Thermal metamorphism has also been attributed to Apollo 14 volcanic rocks 14053 and 14072 undergoing subsolidus alteration, as mentioned above (Taylor et al., 2004).

Vapor-phase metasomatism could have enriched individual mesostasis regions in Cl with minimal effect on their H_2O budgets (if the metasomatic agent was low in H for example), and, at the same time, increased apatite $\delta^{37}Cl$ values. Such mechanism could, therefore, induce

heterogeneous increase of apatite $\delta^{37}Cl$ values and Cl contents depending on the timing and degree of interaction. No strong correlation between apatite Cl and H_2O abundances and $\delta^{37}Cl$ values is expected in this scenario since measured abundances would be variable depending on the initial apatite volatile contents. Such a process could also create variations of apatite volatile abundances and isotopic compositions from grain to grain and from mesostasis area to mesostasis area in a single sample depending on the apatite size or the local permeability, for example. In the case of granulite 79215, Treiman et al. (2014) suggested that the addition of P and halogens due to vapor-phase metasomatism triggered growth of large apatite crystals characterized by homogeneous, elevated $\delta^{37}Cl$ values. Although in this same sample, 79215, Barnes et al. (2016) found variations in $\delta^{37}Cl$ values on the order of ~10 ‰. Furthermore, the Treiman et al. (2014) study suggested apatite crystallization in 79215 was induced from P-rich vapor. Recent work, on S abundances in lunar apatite, has also suggested that metasomatic alteration by a S-Cl-bearing volatile phase is responsible for Cl-S zoning observed in apatite in some mare basalts (Konecke et al., 2017). During the final stages of solidification of the studied Apollo 14 samples, a metasomatic agent could have interacted with the melt, altering Cl isotope ratios and abundances. The large variation in $\delta^{37}Cl$ values could thus suggest that some apatite formed prior to interaction with a metasomatic agent, while others grew after variable metasomatism. It is also plausible that the high-Al basalts assimilated vapor phase products during lava flow on the lunar surface, in a similar way to how variable amounts of KREEP material were assimilated to these basalts (Hui et al., 2011; Hui et al., 2013). This variability in assimilation, and in the original Cl isotope signatures of vapor phase products, could account for the large inter- and intra-sample heterogeneity of Cl isotopes observed in these samples.

It has been suggested that lunar ejecta blankets, such as the Fra Mauro unit, could have initiate non-volcanic fumarole activity (McKay et al., 1972). Vapors released during crystallization within hot zones (~ 1000 °C) percolate up through colder zones where non-condensable gases (i.e. Cl) may escape through the ejecta blanket forming fumaroles (Fig. 6; Shearer et al., 2014). This process has also been identified in 'rusty-rock' 66095 (Shearer et al., 2014) and is similar to the mechanism proposed to explain crystallization of large apatite with elevated δ^{37}Cl values in granulite 79215 (Treiman et al., 2014). Vapor condensation has also been proposed as a mechanism to explain volatile contents in lunar glass beads (74220, 15426) and 66095 (Day et al., 2017). The two samples, 66095 and 79215, have yielded dates around 3.9 Ga (Fischer-Gödde and Becker, 2012; Norman et al., 2006; Snape et al., 2017), similar to the Apollo 14 samples studied here (Table 1). Altogether, these samples hint at the widespread occurrence of vapor-related metasomatism during a period when the impact flux on the lunar surface may have been particularly high (Gomes et al., 2005; Morbidelli et al., 2012; Tera et al., 1974). As samples 66095 and 79215 are from landing sites on the western limb of the nearside, this work extends the geographical occurrence of vapor-rich mestasomatism on the lunar surface to include the Apollo 14 site on the mid-eastern section of the nearside, hinting at large-scale volatile release during this period, possibly related to the Imbrium impact event.

6. Conclusions

Understanding processes that have affected the volatile contents and isotopic compositions of lunar samples is important for constraining the volatile budget of the lunar interior. The Apollo 14 samples studied here have provided an opportunity to explore the various processes that can fractionate Cl isotopes in lunar magmatic and surface environments. The interaction

with a KREEP component, during the Apollo 14 samples petrogenesis, is expected to have imprinted an elevated $\delta^{37}Cl$ signature. Instead, other process(es) must be responsible for the wide-range, elevated, $\delta^{37}Cl$ values of the Apollo 14 samples investigated. We propose that magmatic degassing, as first suggest by Sharp et al. (2010) could explain the elevated $\delta^{37}Cl$ signature of Apollo 14 melts but that this process alone could not account for the variability of isotopic signatures observed in these rocks. The mechanism we ultimately favor, to explain the large intra- and inter-sample variability in $\delta^{37}Cl$ isotope values measured, is variable interaction of late-stage melts with a Cl-rich vapor-phase. The presence of vapor-induced metasomatism in these samples points to the presence of wide-spread fumarolic activity on the nearside of the Moon at ~ 4 Ga.

Acknowledgements

We thank NASA CAPTEM for the allocation of Apollo samples. STFC is thanked for a PhD studentship to N.J.P and a research grant to M.A. and I.A.F. (grant number ST/I001298/1). NanoSIMS access was through UKCAN funded through STFC grant ST/1001964/1. Zachary Sharp and two anonymous reviewers are thanked for their constructive comments.

References

Alexander E. C. and Davis P. K. (1974) 40Ar-39Ar ages and trace element contents of Apollo 14 breccias; an interlaboratory cross-calibration of 40Ar-39Ar standards. *Geochim. Cosmochim. Acta* **38**, 911–928.

Armytage R. M. G., Georg R. B., Savage P. S., Williams H. M. and Halliday A. N. (2011) Silicon isotopes in meteorites and planetary core formation. *Geochim. Cosmochim. Acta* **75**, 3662–3676.

Armytage R. M. G., Georg R. B., Williams H. M. and Halliday A. N. (2012) Silicon isotopes in lunar rocks: Implications for the Moon's formation and the early history of the Earth. *Geochim. Cosmochim. Acta* **77**, 504–514.

Barnes J. D., Sharp Z. D. and Fischer T. P. (2008) Chlorine isotope variations across the Izu-Bonin-Mariana arc. *Geology* **36**, 883.

Barnes J. D., Sharp Z. D., Fischer T. P., Hilton D. R. and Carr M. J. (2009) Chlorine isotope

variations along the Central American volcanic front and back arc. *Geochemistry, Geophys. Geosystems* **10**, 1–17.

Barnes J. J., Franchi I. a., Anand M., Tartèse R., Starkey N. a., Koike M., Sano Y. and Russell S. S. (2013) Accurate and precise measurements of the D/H ratio and hydroxyl content in lunar apatites using NanoSIMS. *Chem. Geol.* **337–338**, 48–55.

Barnes J. J., Tartèse R., Anand M., McCubbin F. M., Franchi I. A., Starkey N. A. and Russell S. S. (2014) The origin of water in the primitive Moon as revealed by the lunar highlands samples. *Earth Planet. Sci. Lett.* **390**, 244–252.

Barnes J. J., Tartèse R., Anand M., McCubbin F. M., Neal C. R. and Franchi I. A. (2016a) Early degassing of lunar urKREEP by crust-breaching impact(s). *Earth Planet. Sci. Lett.* **447**, 84–94.

Barnes J. J., Tartèse R., Anand M., McCubbin F. M., Neal C. R. and Franchi I. A. (2016b) Early volatile degassing on the Moon by a crust-breaching impact event. *Earth Planet. Sci. Lett.*

Bonifacie M., Jendrzejewski N., Agrinier P., Humler E., Coleman M. and Javoy M. (2008) The Chlorine Isotope Composition of Earth's Mantle. *Science (80-.).* **319**, 1518–1520.

Bonnand P., Parkinson I. J. and Anand M. (2016) Mass dependent fractionation of stable chromium isotopes in mare basalts: Implications for the formation and the differentiation of the Moon. *Geochim. Cosmochim. Acta* **175**, 208–221.

Boyce J. W. and Hervig R. L. (2008) Magmatic degassing histories from apatite volatile stratigraphy. *Geology* **36**, 63.

Boyce J. W., Liu Y., Rossman G. R., Guan Y., Eiler J. M., Stolper E. M. and Taylor L. A. (2010) Lunar apatite with terrestrial volatile abundances. *Nature* **466**, 466–9.

Boyce J. W., Tomlinson S. M., McCubbin F. M., Greenwood J. P. and Treiman A. H. (2014) The lunar apatite paradox. *Science* **344**, 400–2.

Boyce J. W., Treiman A. H., Guan Y., Ma C., Eiler J. M., Gross J., Greenwood J. P. and Stolper E. M. (2015) The chlorine isotope fingerprint of the lunar magma ocean. *Sci. Adv.* **1**, 1–8.

Canup Robin M., Visscher Channon, Salmon Julien and Fegley Bruce (2015) Lunar volatile depletion due to incomplete accretion within an impact-generated disk. *Am. Astron. Soc.*

Canup R. M. (2012) Forming a Moon with an Earth-like composition via a giant impact. *Science* **338**, 1052–5.

Charlier B. L. A., Nowell G. M., Parkinson I. J., Kelley S. P., Pearson D. G. and Burton K. W. (2012) High temperature strontium stable isotope behaviour in the early solar system and planetary bodies. *Earth Planet. Sci. Lett.* **329–330**, 31–40.

Compston W., Vernon M. J., Berry H., Rudowski R., Gray C. M. and Ware N. (1972) Apollo 14 mineral ages and the thermal histroy of the Fra Mauro formation. *Lunar Planet. Sci. Conf.* **3**, 1487–1501.

Compston W., Vernon M. J., Berry H., Rudowski R., Gray C. M., Ware N., Chappell B. W. and Kaye M. (1972) Age and Petrogenesis of Apollo 14 Basalts. *Lunar Planet. Sci. Conf.* **3**.

Ćuk M. and Stewart S. T. (2012) Making the Moon from a fast-spinning Earth: a giant impact followed by resonant despinning. *Science* **338**, 1047–52.

Dasch E. ., Shih C.-Y., Bansal B. ., Wiesmann H. and Nyquist L. . (1987) Isotopic analysis of basaltic fragments from lunar breccia 14321: Chronology and petrogenesis of pre-Imbrium mare

volcanism. *Geochim. Cosmochim. Acta* **51**, 3241–3254.

Dauphas N., Chen J. H. and Papanastassiou D. A. (2015) Testing Earth-Moon Isotopic Homogenization with Calcium-48. *Lunar Planet. Sci. Conf.* **46**, 2436.

Day J. M. D., Moynier F. and Shearer C. K. (2017) Late-stage magmatic outgassing from a volatile-depleted Moon. *Proc. Natl. Acad. Sci. U. S. A.* **114**, 9547–9551.

El Goresy A., Ramdohr P. and Taylor L. A. (1971) The geochemistry of the opaque minerals in Apollo 14 crystalline rocks. *Earth Planet. Sci. Lett.* **13**, 121–129.

Elkins-Tanton L. T., Burgess S. and Yin Q.-Z. (2011) The lunar magma ocean : Reconciling the solidification process with lunar petrology and geochronology. *Earth Planet. Sci. Lett.* **304**, 326–336.

Fegley B. (1991) Thermodynamic models of the chemistry of lunar volcanic gases. *Geophys. Res. Lett.* **18**, 2073–2076.

Fischer-Gödde M. and Becker H. (2012) Osmium isotope and highly siderophile element constraints on ages and nature of meteoritic components in ancient lunar impact rocks. *Geochim. Cosmochim. Acta* **77**, 135–156.

Gola A. A., D'Anna B., Feilberg K. L., Sellevåg S. R., Bache-Andreassen L. and Nielsen C. J. (2005) Kinetic isotope effects in the gas phase reactions of OH and Cl with CH3Cl, CD3Cl, and13CHCl. *Atmos. Chem. Phys.* **5**, 2395–2402.

Gomes R., Levison H. F., Tsiganis K. and Morbidelli A. (2005) Origin of the cataclysmic Late Heavy Bombardment period of the terrestrial planets. *Nature* **435**, 466–469.

Greenwood J. P., Itoh S., Sakamoto N., Warren P., Taylor L. and Yurimoto H. (2011) Hydrogen isotope ratios in lunar rocks indicate delivery of cometary water to the Moon. *Nat. Geosci.* **4**, 79–82.

Hauri E. H., Saal A. E., Rutherford M. J. and Van Orman J. A. (2015) Water in the Moon's interior: Truth and consequences. *Earth Planet. Sci. Lett.* **409**, 252–264.

Herwartz D., Pack A., Friedrichs B. and Bischoff A. (2014) Identification of the giant impactor Theia in lunar rocks. *Science* **344**, 1146–50.

Herzog G. F., Moynier F., Albarède F. and Berezhnoy A. A. (2009) Isotopic and elemental abundances of copper and zinc in lunar samples, Zagami, Pele's hairs, and a terrestrial basalt. *Geochim. Cosmochim. Acta* **73**, 5884–5904.

Hiesinger H. and Head J. W. (2006) New Views of Lunar Geoscience: An Introduction and Overview. *Rev. Mineral. Geochemistry* **60**, 1–81.

Huang L., Sturchio N. ., Abrajano T., Heraty L. . and Holt B. . (1999) Carbon and chlorine isotope fractionation of chlorinated aliphatic hydrocarbons by evaporation. *Org. Geochem.* **30**, 777–785.

Hui H., Neal C. R., Shih C.-Y. and Nyquist L. E. (2013) Petrogenetic association of the oldest lunar basalts: Combined Rb–Sr isotopic and trace element constraints. *Earth Planet. Sci. Lett.* **373**, 150–159.

Hui H., Oshrin J. G. and Neal C. R. (2011) Investigation into the petrogenesis of Apollo 14 high-Al basaltic melts through crystal stratigraphy of plagioclase. *Geochim. Cosmochim. Acta* **75**, 6439–6460.

Husain L., Sutter J. F. and Schaeffer O. A. (1971) Ages of crystalline rocks from fra mauro. *Science*

173, 1235–6.

Kato C., Moynier F., Valdes M. C., Dhaliwal J. K. and Day J. M. D. (2015) Extensive volatile loss during formation and differentiation of the Moon. *Nat. Commun.* **6**, 7617.

Kaufmann R., Long A., Bentley H. and Davis S. (1984) Natural chlorine isotope variations. *Nature* **309**, 338–340.

Konecke B. A., Fiege A., Simon A. C. and Holtz F. (2017) Cryptic metasomatism during late-stage lunar magmatism implicated by sulfur in apatite. *Geology* **45**, G39249.1.

Krähenbühl U., Ganapathy R., Morgan J. W. and Anders E. (1973) Volatile elements in Apollo 16 samples: Implications for highland volcanism and accretion history of the moon. *Lunar Planet. Sci. Conf.* **4**, 1325.

Kusebauch C., John T., Whitehouse M. J., Klemme S. and Putnis A. (2015) Distribution of halogens between fluid and apatite during fluid-mediated replacement processes. *Geochim. Cosmochim. Acta* **170**, 225–246.

Liebscher A., Barnes J. and Sharp Z. (2006) Chlorine isotope vapor–liquid fractionation during experimental fluid-phase separation at 400 °C/23 MPa to 450 °C/42 MPa. *Chem. Geol.* **234**, 340–345.

Lugmair G. W. and Shukolyukov A. (1998) Early solar system timescales according to 53Mn-53Cr systematics. *Geochim. Cosmochim. Acta* **62**, 2863–2886.

Mark R. K., Lee-Hu C.-N. and Weatherill G. W. (1974) Rb-Sr age of lunar igneous rocks 62295 and 14310. *Geochim. Cosmochim. Acta* **38**, 1643–1648.

McCubbin F. M., Jolliff B. L., Nekvasil H., Carpenter P. K., Zeigler R. a., Steele A., Elardo S. M. and Lindsley D. H. (2011) Fluorine and chlorine abundances in lunar apatite: Implications for heterogeneous distributions of magmatic volatiles in the lunar interior. *Geochim. Cosmochim. Acta* **75**, 5073–5093.

McCubbin F. M., Vander Kaaden K. E., Tartèse R., Boyce J. W., Mikhail S., Whitson E. S., Bell A. S., Anand M., Franchi I. A., Wang J. and Hauri E. H. (2015) Experimental investigation of F, Cl, and OH partitioning between apatite and Fe-rich basaltic melt at 1.0 to 1.2 GPa and 950 to 1000 °C. *Am. Mineral.* **100**, 1790–1802.

McCubbin F. M., Vander Kaaden K. E., Tartèse R., Klima R. L., Liu Y., Mortimer J., Barnes J. J., Shearer C. K., Treiman A. H., Lawrence D. J., Elardo S. M., Hurley D. M., Boyce J. W. and Anand M. (2015) Magmatic volatiles (H, C, N, F, S, Cl) in the lunar mantle, crust, and regolith: Abundances, distributions, processes, and reservoirs. *Am. Mineral.* **100**, 1668–1707.

McCubbin F. M., Steele A., Hauri E. H., Nekvasil H., Yamashita S. and Hemley R. J. (2010) Nominally hydrous magmatism on the Moon. *Proc. Natl. Acad. Sci. U. S. A.* **107**, 11223–8.

McCubbin F. M., Steele A., Nekvasil H., Schnieders A., Rose T., Fries M., Carpenter P. K. and Jolliff B. L. (2010) Detection of structurally bound hydroxyl in fluorapatite from Apollo Mare basalt 15058,128 using TOF-SIMS. *Am. Mineral.* **95**, 1141–1150.

McKay D. S., Clanton U. S., Heiken G. H., Morrison D. A., Taylor R. M. and Ladle G. (1972) Vapor Phase Crystallization in Apollo 14 Breccias and Size Analysis of Apollo 14 Soils. *Lunar Planet. Sci. Conf.* **3**, 529.

McKay G. A., McKay G. A., Wiesmann H., Bansal B. M. and Shih C.-Y. (1979) Petrology, chemistry, and chronology of Apollo 14 KREEP basalts. *Lunar Planet. Sci. Conf.* **10**, 181–205.

Meyer C., Williams I. S. and Compston W. (1996) Uranium-lead ages for lunar zircons: Evidence for a prolonged period of granophyre formation from 4.32 to 3.88 Ga. *Meteorit. Planet. Sci.* **31**, 370–387.

Morbidelli A., Marchi S., Bottke W. F. and Kring D. A. (2012) A sawtooth-like timeline for the first billion years of lunar bombardment. *Earth Planet. Sci. Lett.* **355**, 144–151.

Neal C. R. and Kramer G. Y. (2006) The petrogenesis of the Apollo 14 high-Al mare basalts. *Am. Mineral.* **91**, 1521–1535.

Neal C. R. and Taylor L. A. (1989) Metasomatic products of the lunar magma ocean: The role of KREEP dissemination. *Geochim. Cosmochim. Acta* **53**, 529–541.

Neal C. R., Taylor L. A. and Lindstrom M. M. (1988) Apollo 14 mare basalt petrogenesis - Assimilation of KREEP-like components by a fractionating magma. *Lunar Planet. Sci. Conf.* **18**, 139–153.

Neal C. R., Taylor L. A., Schmitt R. A., Hughes S. S. and Lindstrom M. M. (1989) High alumina (HA) and very high potassium (VHK) basalt clasts from Apollo 14 breccias. II - Whole rock geochemistry - Further evidence for combined assimilation and fractional crystallization within the lunar crust. *Lunar Planet. Sci. Conf.* **19**, 147–161.

Nemchin A. A., Pidgeon R. T., Healy D., Grange M. L., Whitehouse M. J. and Vaughan J. (2009) The comparative behavior of apatite-zircon U-Pb systems in Apollo 14 breccias: Implications for the thermal history of the Fra Mauro Formation. *Meteorit. Planet. Sci.* **44**, 1717–1734.

Nemchin A. A., Pidgeon R. T., Whitehouse M. J., Vaughan J. P. and Meyer C. (2008) SIMS U–Pb study of zircon from Apollo 14 and 17 breccias: Implications for the evolution of lunar KREEP. *Geochim. Cosmochim. Acta* **72**, 668–689.

Nemchin A., Grange M. and Pidgeon R. (2010) Distribution of rare earth elements in lunar zircon. *Am. Astron. Soc.* **95**, 273–283.

Norman M. D., Duncan R. A. and Huard J. J. (2006) Identifying impact events within the lunar cataclysm from 40Ar–39Ar ages and compositions of Apollo 16 impact melt rocks. *Geochim. Cosmochim. Acta* **70**, 6032–6049.

Nunes P. D. and Tatsumoto M. (1973) Excess lead in rusty rock 66095 and implications for an early lunar differentiation. *Science* **182**, 916–20.

Paniello R. C., Day J. M. D. and Moynier F. (2012) Zinc isotopic evidence for the origin of the Moon. *Nature* **490**, 376–9.

Papanastassiou D. A. and Wasserburg G. J. (1971) RbSr ages of igneous rocks from the Apollo 14 mission and the age of the Fra Mauro formation. *Earth Planet. Sci. Lett.* **12**, 36–48.

Patiño Douce A. E. and Roden M. (2006) Apatite as a probe of halogen and water fugacities in the terrestrial planets. *Geochim. Cosmochim. Acta* **70**, 3173–3196.

Richet P., Bottinga Y. and Javoy M. (1977) A review of hydrogen, carbon, nitrogen, oxygen, sulphur, and chlorine stable isotope fractionation amoung gaseous molecules. *Annu. Rev. Earth Planet. Sci.* **5**, 65–110.

Ridley W. I. (1975) On high-alumina mare basalts. *Lunar Sci. Conf.* **6**, 131–145.

Robinson K. L., Barnes J. J., Nagashima K., Thomen A., Franchi I. A., Huss G. R., Anand M. and Taylor G. J. (2016) Water in evolved lunar rocks: Evidence for multiple reservoirs. *Geochim. Cosmochim. Acta* **188**, 244–260.

Rubie D. C., Jacobson S. a., Morbidelli a., O'Brien D. P., Young E. D., de Vries J., Nimmo F., Palme H. and Frost D. J. (2015) Accretion and differentiation of the terrestrial planets with implications for the compositions of early-formed Solar System bodies and accretion of water. *Icarus* **248**, 89–108.

Saal A. E., Hauri E. H., Van Orman J. a and Rutherford M. J. (2013) Hydrogen isotopes in lunar volcanic glasses and melt inclusions reveal a carbonaceous chondrite heritage. *Science* **340**, 1317–20.

Schauble E. A., Rossman G. R., Taylor, H. P. J. and Taylor H. . (2003) Theoretical estimates of equilibrium chlorine-isotope fractionations. *Geochim. Cosmochim. Acta* **67**, 3267–3281.

Schönbächler M., Lee D.-C., Rehkämper M., Halliday A. N., Fehr M. A., Hattendorf B. and Günther D. (2003) Zirconium isotope evidence for incomplete admixing of r-process components in the solar nebula. *Earth Planet. Sci. Lett.* **216**, 467–481.

Schonfeld E. and Meyer, Charles J. (1972) The abundances of components of the lunar soils by a least-squares mixing model and the formation age of KREEP. *Lunar Planet. Sci. Conf.* **3**, 1397.

Sharp Z., Barnes J., Fischer T. and Halick M. (2010) An experimental determination of chlorine isotope fractionation in acid systems and applications to volcanic fumaroles. *Geochim. Cosmochim. Acta* **74**, 264–273.

Sharp Z. D., Barnes J. D., Brearley A. J., Chaussidon M., Fischer T. P. and Kamenetsky V. S. (2007) Chlorine isotope homogeneity of the mantle, crust and carbonaceous chondrites. *Nature* **446**, 1062–5.

Sharp Z. D. D., Mercer J. A. A., Jones R. H. H., Brearley A. J. J., Selverstone J., Bekker A. and Stachel T. (2013) The Chlorine Isotope Composition of Chondrites and Earth. *Geochim. Cosmochim. Acta* **107**, 189–204.

Sharp Z. D., Shearer C. K., McKeegan K. D., Barnes J. D. and Wang Y. Q. (2010) The chlorine isotope composition of the moon and implications for an anhydrous mantle. *Science* **329**, 1050–3.

Shearer C. K., Hess P. C., Wieczorek M. A., Pritchard M. E., Parmentier E. M., Borg L. E., Longhi J., Elkins-Tanton L. T., Neal C. R., Antonenko I., Canup R. M., Halliday A. N., Grove T. L., Hager B. H., Lee D.-C. and Wiechert U. (2006) Thermal and Magmatic Evolution of the Moon. *Rev. Mineral. Geochemistry* **60**, 365–518.

Shearer C. K., Sharp Z. D., Burger P. V., McCubbin F. M., Provencio P. P., Brearley A. J. and Steele A. (2014) Chlorine distribution and its isotopic composition in "rusty rock" 66095. Implications for volatile element enrichments of "rusty rock" and lunar soils, origin of "rusty" alteration, and volatile element behavior on the Moon. *Geochim. Cosmochim. Acta* **139**, 411–433.

Shinohara H. (2009) A missing link between volcanic degassing and experimental studies on chloride partitioning. *Chem. Geol.* **263**, 51–59.

Snape J. F., Nemchin A. A., Bellucci J. J. and Whitehouse M. J. (2017) Pb isotopes in the impact melt breccia 66095: Association with the Imbrium basin and the isotopic composition of lithologies at the Apollo 16 landing site. *Chem. Geol.* **466**, 608–616.

Snape J. F., Nemchin A. A., Grange M. L., Bellucci J. J., Thiessen F. and Whitehouse M. J. (2016) Phosphate ages in Apollo 14 breccias: Resolving multiple impact events with high precision U–Pb SIMS analyses. *Geochim. Cosmochim. Acta* **174**, 13–29.

Snyder G. A., Borg L. E., Nyquist L. E. and Taylor L. A. (2000) Chronology and Isotopic Constraints on Lunar Evolution. In *Origin of the earth and moon* (eds. R. M. Canup and K. Righter).

Tucson: University of Arizona Press. pp. 361–395.

Stöffler D. and Ryder G. (2001) Stratigraphy and Isotope Ages of Lunar Geologic Units: Chronological Standard for the Inner Solar System. *Space Sci. Rev.* **96**, 9–54.

Tartèse R., Anand M., Barnes J. J., Starkey N. A., Franchi I. A. and Sano Y. (2013) The abundance, distribution, and isotopic composition of Hydrogen in the Moon as revealed by basaltic lunar samples: Implications for the volatile inventory of the Moon. *Geochim. Cosmochim. Acta* **122**, 58–74.

Tartèse R., Anand M., Joy K. H. and Franchi I. A. (2014) H and Cl isotope systematics of apatite in brecciated lunar meteorites Northwest Africa 4472, Northwest Africa 773, Sayh al Uhaymir 169, and Kalahari 009. *Meteorit. Planet. Sci.* **49**, 2266–2289.

Tartèse R., Anand M., McCubbin F. M., Elardo S. M., Shearer C. K. and Franchi I. A. (2014) Apatites in lunar KREEP basalts: The missing link to understanding the H isotope systematics of the Moon. *Geology* **42**, 363–366.

Tartèse R., Anand M., McCubbin F. M., Elardo S. M., Shearer C. K. and Franchi I. A. (2014) Apatites in lunar KREEP basalts: The missing link to understanding the H isotope systematics of the Moon. *Geology* **42**, 363–366.

Tatsumoto M., Hedge C. E., Doe B. R. and Unruh D. M. (1972) U-Th-Pb and Rb-Sr measurements on some Apollo 14 lunar samples. *Lunar Planet. Sci. Conf.* **3**, 1531.

Taylor L. A., Patchen A., Mayne R. G. and Taylor D.-H. (2004) The most reduced rock from the moon , Apollo 14 basalt 14053 : Its unique features and their origin. *Am. Mineral.* **89**, 1617–1624.

Tera F., Papanastassiou D. A. and Wasserburg G. J. (1974) Isotopic evidence for a terminal lunar cataclysm. *Earth Planet. Sci. Lett.* **22**, 1–21.

Treiman A. H., Boyce J. W., Gross J., Guan Y., Eiler J. M. and Stolper E. M. (2014) Phosphate-halogen metasomatism of lunar granulite 79215: Impact-induced fractionation of volatiles and incompatible elements. *Am. Mineral.* **99**, 1860–1870.

Turner G., Huneke J. C., Podosek F. A. and Wasserburg G. J. (1971) 40Ar-39Ar ages and cosmic ray exposure ages of Apollo 14 samples. *Earth Planet. Sci. Lett.* **12**, 19–35.

Turner G., Huneke J. C., Podosek F. A. and Wasserburg G. J. (1972) Ar40-Ar30 systematics in rocks and separated minerals from Apollo 14. *Lunar Planet. Sci. Conf.* **3**, 1589–1612.

Ustunisik G., Nekvasil H. and Lindsley D. (2011) Differential degassing of H2O, Cl, F, and S: Potential effects on lunar apatite. *Am. Mineral.* **96**, 1650–1653.

Ustunisik G., Nekvasil H., Lindsley D. H. and McCubbin F. M. (2015) Degassing pathways of Cl-, F-, H-, and S-bearing magmas near the lunar surface: Implications for the composition and Cl isotopic values of lunar apatite. *Am. Mineral.* **100**, 1717–1727.

Valdes M. C., Moreira M., Foriel J. and Moynier F. (2014) The nature of Earth's building blocks as revealed by calcium isotopes. *Earth Planet. Sci. Lett.* **394**, 135–145.

Wang K. and Jacobsen S. B. (2016) Potassium isotopic evidence for a high-energy giant impact origin of the Moon. *Nature* **538**, 487–490.

Warren P. H. and Wasson J. T. (1979) The origin of KREEP. *Rev. Geophys.* **17**, 73.

Webster J. D., Kinzler R. J. and Mathez E. A. (1999) Chloride and water solubility in basalt and

andesite melts and implications for magmatic degassing. *Geochim. Cosmochim. Acta* **63**, 729–738.

Webster J. D., Tappen C. M. and Mandeville C. W. (2009) Partitioning behavior of chlorine and fluorine in the system apatite–melt–fluid. II: Felsic silicate systems at 200MPa. *Geochim. Cosmochim. Acta* **73**, 559–581.

Wetzel D. T., Hauri E. H., Saal A. E. and Rutherford M. J. (2015) Carbon content and degassing history of the lunar volcanic glasses. *Nat. Geosci.* **8**, 755–758.

Wiechert U., Halliday A. N., Lee D. C., Snyder G. A., Taylor L. A. and Rumble D. (2001) Oxygen isotopes and the moon-forming giant impact. *Science* **294**, 345–8.

Wieczorek M. A., Neumann G. A., Nimmo F., Kiefer W. S., Taylor G. J., Melosh H. J., Phillips R. J., Solomon S. C., Andrews-Hanna J. C., Asmar S. W., Konopliv A. S., Lemoine F. G., Smith D. E., Watkins M. M., Williams J. G. and Zuber M. T. (2013) The crust of the Moon as seen by GRAIL. *Science* **339**, 671–5.

Wilhelms D. E., McCauley J. F. with sections by and Trask N. J. (1987) *The geologic history of the Moon*.,

York D., Kenyon W. J. and Doyle R. J. (1972) 40Ar-39Ar ages of Apollo 14 and 15 samples. *Lunar Planet. Sci. Conf.* **3**, 1613.

Young E. D., Kohl I. E., Warren P. H., Rubie D. C., Jacobson S. A. and Morbidelli A. (2016) Oxygen isotopic evidence for vigorous mixing during the Moon-forming giant impact. *Science (80-.).* **351**, 493–496.

Zambardi T., Poitrasson F., Corgne A., Méheut M., Quitté G. and Anand M. (2013) Silicon isotope variations in the inner solar system: Implications for planetary formation, differentiation and composition. *Geochim. Cosmochim. Acta* **121**, 67–83.

Zhang J., Dauphas N., Davis A. M., Leya I. and Fedkin A. (2012) The proto-Earth as a significant source of lunar material. *Nat. Geosci.* **5**, 251–255.

Figure Captions

Figure 1: Ternary diagram of apatite X-site occupancy (mol%), assuming that X-site is completely filled with F + Cl + H_2O. F was calculated by difference for all analyses expect those with F abundances reported in Table 3. Literature data from McCubbin et al., (2015), and references therein.

Figure 2: $\delta^{37}Cl$ data for volcanic samples (see text) 14053, 14072, and 14321,1482 plotted against (A) Cl and (B) H_2O abundances, and for impact melt samples (see text) 14073 and 14310 plotted against (C) Cl concentration (D) H_2O abundances.

Figure 3: All available $\delta^{37}Cl$ data plotted against (A) H_2O (ppm), and (B) Cl (ppm) with fields for literature data.. Literature data from Barnes et al. (2016), Boyce et al. (2015), Tartèse et al. (2014a), Treiman et al. (2014), and Sharp et al. (2010). NWA refers to KREEP-rich clast in NWA4472 from Tartèse et al. (2014b). Note the difference in VHK and granulite fields between A and B result from the highest $\delta^{37}Cl$ values for each rock type not having H_2O abundance associated with them.

Figure 4: All available $\delta^{37}Cl$ data for Apollo samples plotted against bulk rock La/Lu. La and Lu abundances averaged from data taken from Lunar Sample Compendium. References are given in SM1 Table 1. Literature data from Barnes et al. (2016), Boyce et al. (2015), Treiman et al. (2014), and Sharp et al. (2010). '14321' refers to 14321,1482.

Figure 5: F abundance of apatite (wt.%) plotted against $\delta^{37}Cl$ values for samples in this study. F contents are those either measured (see Table 2) or calculated by difference assuming the X-site is completely filled with F + Cl + H_2O. '14321' refers to 14321,1482.

Figure 6: Schematic diagram of vapor-release metasomatism following impact-events or emplacement of lava flows. After an impact-event or volcanic eruption, a hot zone (~1000 °C) develops underneath the ejecta blanket/lava flow. As crystallization occurs in this hot zone, vapors are released. These vapors travel up through the solidifying ejector blanket/lava flow allowing for vapor interaction with warmed-up/solidifying rock. Cartoon after Shearer et al. (2014) and McKay et al. (1972).

Figure 1

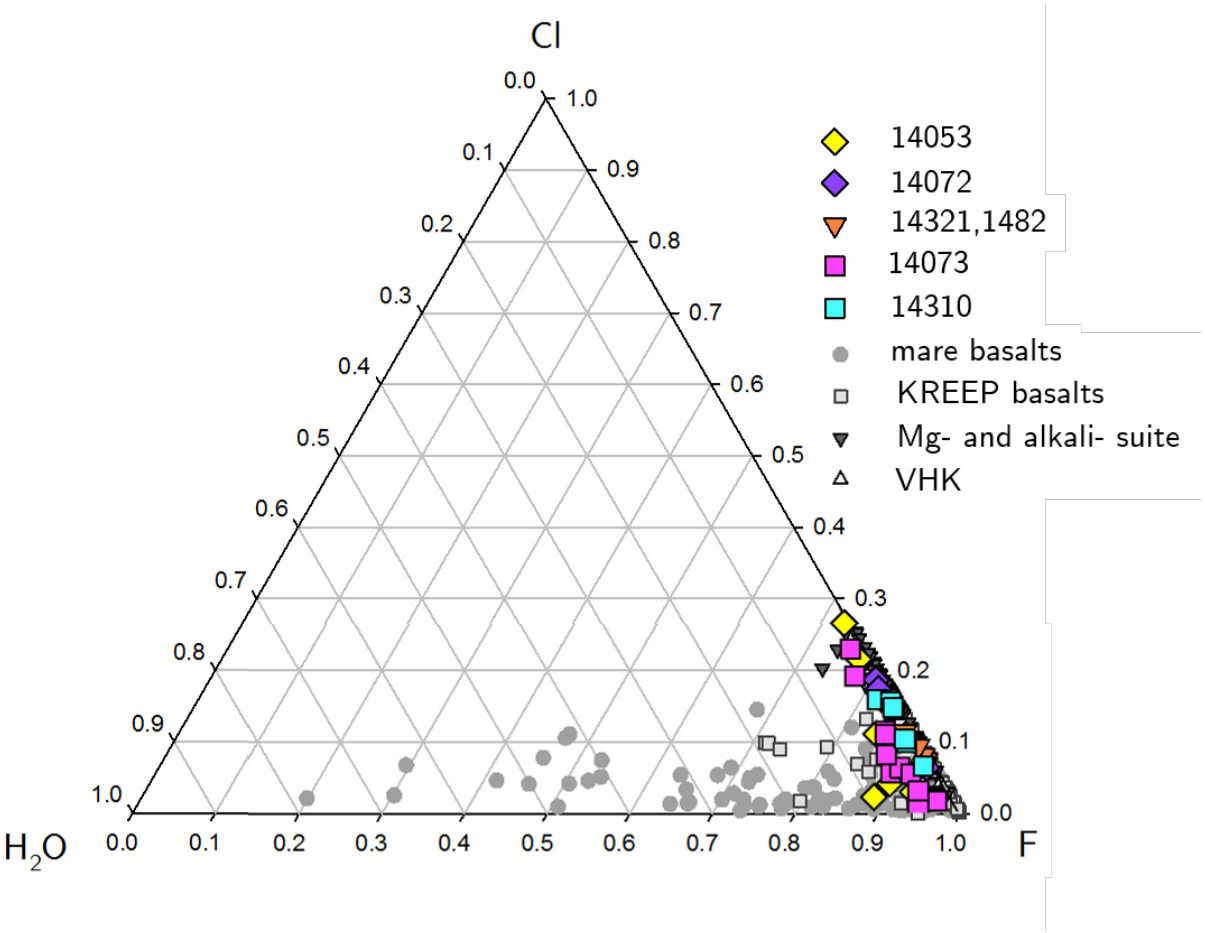
Cl
H2O
F
0.0
0.1
0.2
0.3
0.4
0.5
0.6
0.7
0.8
0.9
1.0
14053
14072
14321,1482
14073
14310
mare basalts
KREEP basalts
Mg- and alkali- suite
VHK

Figure 2

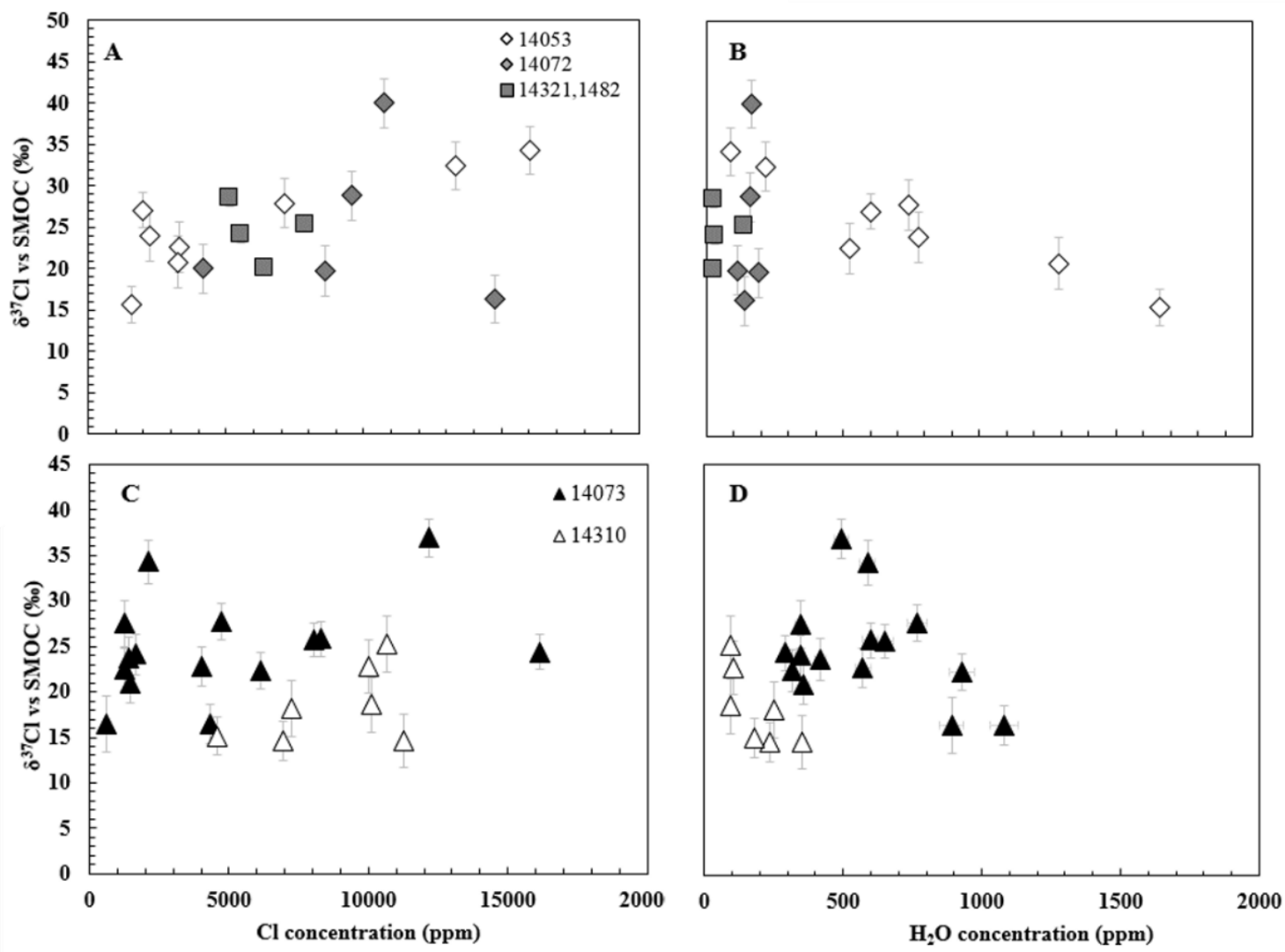
A
B
C
D
14053
14072
14321,1482
14073
14310
δ37Cl vs SMOC (‰)
Cl concentration (ppm)
H2O concentration (ppm)
0
5
10
15
20
25
30
35
40
45
50
0
5000
10000
15000
2000
500
1000
1500

Figure 3

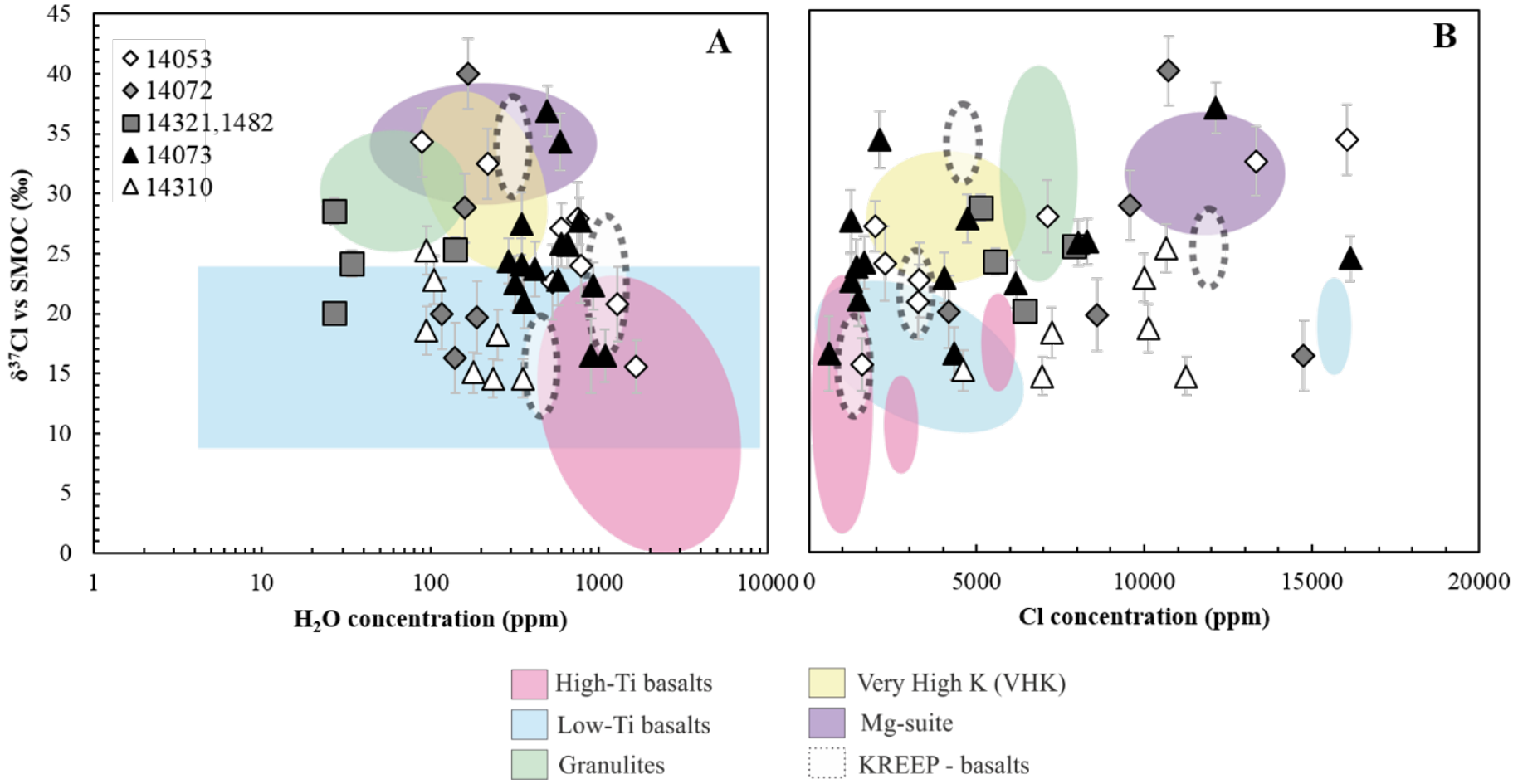
A
B
14053
14072
14321,1482
14073
14310
δ37Cl vs SMOC (‰)
H2O concentration (ppm)
Cl concentration (ppm)
High-Ti basalts
Low-Ti basalts
Granulites
Very High K (VHK)
Mg-suite
KREEP - basalts

Figure 4

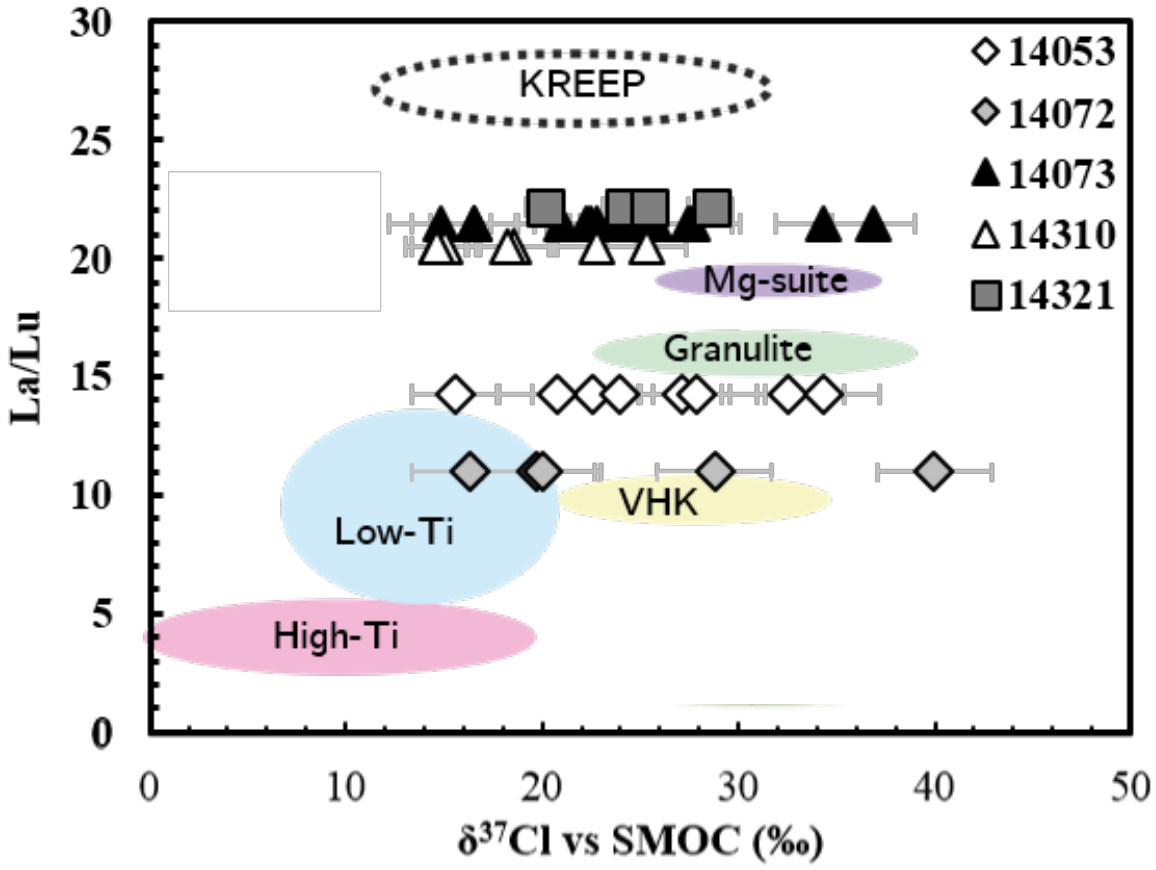
30
25
20
15
10
5
0
La/Lu
0
10
20
30
40
50
δ37Cl vs SMOC (‰)
KREEP
Mg-suite
Granulite
VHK
Low-Ti
High-Ti
14053
14072
14073
14310
14321

Figure 5

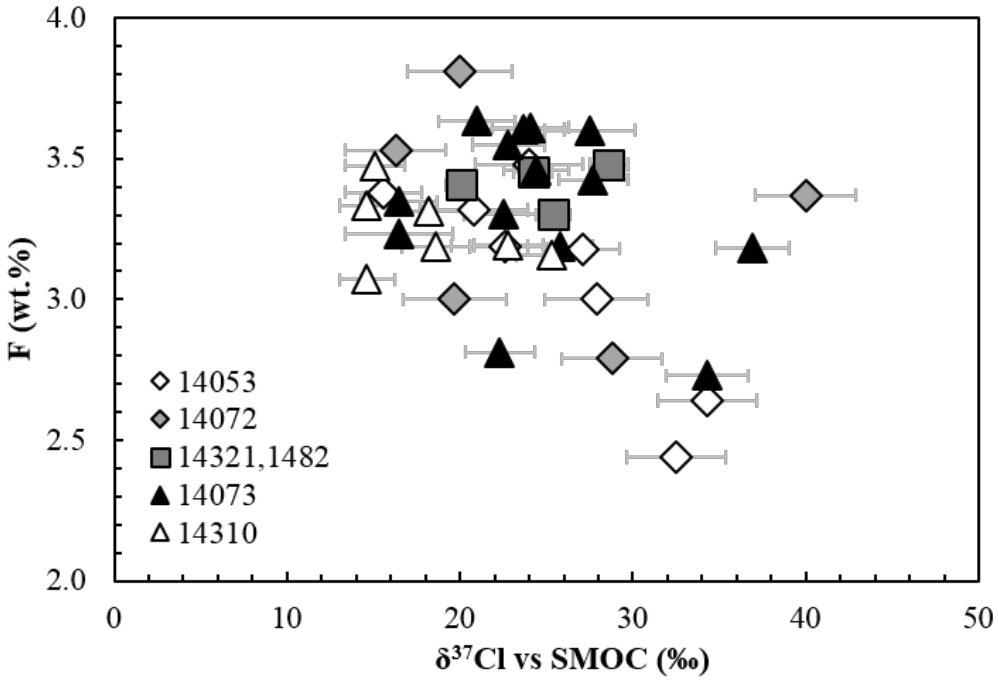
4.0
3.5
3.0
2.5
2.0
F (wt.%)
0
10
20
30
40
50
δ37Cl vs SMOC (‰)
14053
14072
14321,1482
14073
14310

Figure 6

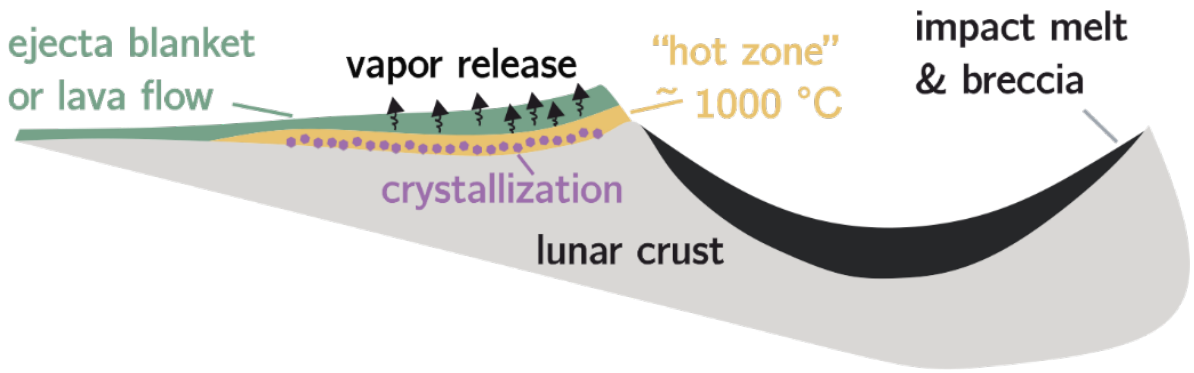
ejecta blanket
or lava flow
vapor release
"hot zone"
~ 1000 °C
impact melt
& breccia
crystallization
lunar crust

Table 1: Radiometric dates obtained for Apollo 14 samples studied here and their geochemical grouping. All dates are in Ga. Data from a) Husain et al. (1971), b) Papanastassiou and Wasserburg (1971), c) York et al. (1972), d) Compston et al. (1972b), e) Dasch et al. (1987), f) Turner et al. (1972), g) Mark et al. (1974), and h) Tatsumoto et al. (1972). *Rb-Sr data re-processed with updated decay constant, all dates from Hui et al. (2013). **14072 does not belong to any group of high-Al basalts but is geochemically intermediate between Group A and C. Note a crystallization age of 3905 ± 8 Ma has also been determined for 14072 from Pb/Pb dating by Snape et al. (2016).

	Ages			Geochemical Features	
	$^{40}Ar/^{39}Ar$	Rb-Sr	Rb-Sr*	Group	Crystallization
14053	3.92 ± 0.08[a]	3.96 ± 0.04[b]	3.94 ± 0.03	C	open
14072	4.04 ± 0.05[c]	3.99 ± 0.09[d]	3.98 ± 0.15	A – C**	open
			3.98 ± 0.09		
14321,1482				B	open
14073	3.88 ± 0.05[e]	3.88 ± 0.04[a]	3.86 ± 0.02	impact melt	closed
14310	3.88 ± 0.05[f]	3.94 ± 0.03[g]	3.85 ± 0.02	impact melt	closed
		3.84 ± 0.04[h]	3.92 ± 0.06		
			3.90 ± 0.19		

Table 2: Measured Cl isotopic values (‰), and background corrected Cl (ppm), H_2O (ppm), and F (wt.%) abundances of apatite in the Apollo 14 samples analyzed in this study. (B) and (C) refer to Fig.2 panel for 14072,13.

Sample	$\delta^{37}Cl$ (‰)	2σ (‰)	Cl (ppm)	2σ (ppm)	H_2O (ppm)	2σ (ppm)	F (wt.%)	2σ (‰)
Sample 14053,19								
14053_A1_Ap#1	15.6	2.2	1569	2	1662	80	3.38	0.04
14053_A1_Ap#2	27.1	2.1	1967	2	601	29	3.18	0.03
14053_A4_Ap#4a	34.3	2.9	16054	17	89	4.3	2.64	0.03
14053_A4_Ap#4b	32.5	2.9	13332	14	218	11	2.44	0.03
14053_A5_Ap#5a	22.6	3.1	3292	4	526	25	3.19	0.03
14053_A5_Ap#5b	27.9	3.0	7109	8	743	36	3.00	0.03
14053_A8_Ap#8a	24.0	3.1	2251	3	779	38		
14053_A8_Ap#8b	20.8	3.1	3263	4	1292	62		
Sample 14072,13								
14072_A7_Ap#3	19.7	3.0	8589	10	189	9	3.00	0.03
14072_A3_Ap#1(B)	16.3	2.9	14759	15	140	7	3.53	0.04
14072_A3_Ap#1(C)	20.0	3.0	4167	5	117	6		
14072_A4_Ap#1	40.0	2.9	10737	12	167	8	3.37	0.04
14072_A6_Ap#1	28.8	2.9	9580	11	160	8	2.79	0.03
Sample 14321,1482								
14321,1482_A3_Ap1a	28.6	1.1	5117	9	27	1		
14321,1482_A3_Ap1b	24.2	1.1	5549	10	34	1		
14321,1482_A4_Ap1a	25.4	1.0	7897	14	140	5		
14321,1482_A5_Ap2a	20.1	0.9	6414	10	27	1		

Sample 14073,9								
14073_A11_Ap#1	27.5	2.6	1241	2	346	17	3.04	0.03
14073_A11_Ap#2	23.7	2.3	1421	2	419	20		
14073_A11_Ap#3	24.1	2.2	1648	2	346	17		
14073_A11_Ap#4	21.0	2.2	1479	2	360	17		
14073_A11_Ap#5	22.5	2.3	1254	2	317	15		
14073_A12_Ap#a	16.5	2.2	4317	5	1081	52		
14073_A12_Ap#b	27.7	2.0	4713	5	766	37		
14073_A12_Ap#c	22.8	2.1	4021	5	572	28		
14073_A12_Ap#d	16.5	3.1	580	1	893	43		
14073_A17_Ap#a	22.3	2.0	6157	7	929	45		
14073_A17_Ap#b	24.4	1.9	16149	18	291	14		
14073_A18_Ap#a	34.3	2.4	2097	3	588	28	3.46	0.04
14073_A19_Ap#a	36.9	2.1	12146	13	493	24	2.73	0.03
14073_A19_Ap#b	25.8	1.9	8311	9	598	29		
14073_A19_Ap#c	25.7	1.9	8033	8	649	31		
Sample 14310,171								
14310_A1_Ap#1	14.6	1.6	6962	12	243	8		
14310_A1_Ap#2	15.1	1.7	4597	8	179	6		
14310_A2_Ap#1a	14.6	1.6	11256	19	354	11		
14310_A2_Ap#1b	22.8	2.0	9992	18	105	4		
14310_A2_Ap#1c	25.3	2.0	10654	19	95	3		
14310_A2_Ap#2	18.6	2.0	10121	19	95	3		
14310_A5_Ap#1	18.2	2.1	7238	13	251	8		

16